

Physics-Guided Tiny-Mamba Transformer for Reliability-Aware Early Fault Warning

Changyu Li^{1,3}, Dingcheng Huang², Kexuan Yao³, Xiaoya Ni⁴, Lijuan Shen⁵, and Fei Luo¹

Abstract—Reliability-centered prognostics for rotating machinery requires early warning signals that remain accurate under nonstationary operating conditions, domain shifts across speed/load/sensors, and severe class imbalance, while keeping the false-alarm rate small and predictable. We propose the Physics-Guided Tiny-Mamba Transformer (PG-TMT), a compact tri-branch encoder tailored for online condition monitoring. A depthwise-separable convolutional stem captures micro-transients, a Tiny-Mamba state-space branch models near-linear long-range dynamics, and a lightweight local Transformer encodes cross-channel resonances. We derive an analytic temporal-to-spectral mapping that ties the model’s attention spectrum to classical bearing fault-order bands, yielding a band-alignment score that quantifies physical plausibility and provides physics-grounded explanations. To ensure decision reliability, healthy-score exceedances are modeled with extreme-value theory (EVT), which yields an on-threshold achieving a target false-alarm intensity (events/hour); a dual-threshold hysteresis with a minimum hold time further suppresses chatter. Under a leakage-free streaming protocol with right-censoring of missed detections on CWRU, Paderborn, XJTU-SY, and an industrial pilot, PG-TMT attains higher precision-recall AUC (primary under imbalance), competitive or better ROC AUC, and shorter mean time-to-detect at matched false-alarm intensity, together with strong cross-domain transfer. By coupling physics-aligned representations with EVT-calibrated decision rules, PG-TMT delivers calibrated, interpretable, and deployment-ready early warnings for reliability-centric prognostics and health management.

Index Terms—Prognostics and health management (PHM); reliability-aware early fault warning; survival analysis and right-censoring; extreme value theory (EVT); calibration and uncertainty; state-space models (Tiny-Mamba); Transformers; domain adaptation.

I. INTRODUCTION

EARLY fault warning for rotating machinery is essential for avoiding unplanned outages, safety incidents, and costly secondary damage. Bearings and gears operate over long horizons under varying speed and load, often in tightly coupled production lines. Small changes in detection delay or false-alarm frequency can translate into substantial differences in uptime and maintenance cost [1]–[3]. In modern

Corresponding authors: Lijuan Shen; Fei Luo.

¹Great Bay University, Dongguan, China (e-mail: changyu.li@my.jcu.edu.au; luofei@gbu.edu.cn).

²Massachusetts Institute of Technology, Cambridge, MA 02139 USA (e-mail: dean1231@mit.edu).

³Zhejiang University, Hangzhou 310027, China (e-mail: 12324032@zju.edu.cn).

⁴National University of Singapore, Singapore 119077 (e-mail: e1520186@u.nus.edu).

⁵James Cook University, Singapore 387380 (e-mail: lijuan.shen@jcu.edu.au).

Dingcheng Huang and Kexuan Yao contributed equally to this work.

plants, monitoring is inherently *online*: vibration streams arrive continuously, operating conditions drift, and fault data remain scarce relative to healthy operation. In this setting, practitioners need alarms that are accurate and *calibrated*, expose a tunable false-alarm *intensity* (events/hour), and offer interpretable evidence to support maintenance decisions [42]–[44], [47].

Early fault diagnosis methods for rotating machinery broadly fall into two families. Physics-based approaches, rooted in classical vibration analysis, describe resonance belts and defect-order harmonics using lumped-parameter dynamics, cyclostationarity, and order tracking; they remain closely aligned with engineering intuition and field practice [4]–[7], [31]. Data-driven encoders—including convolutional, recurrent, Transformer, and state-space models—learn temporal-spectral features directly from waveforms and can achieve strong *offline* accuracy on benchmark datasets [8]–[12]. This complementarity has motivated physics-guided learning that injects mechanistic priors into neural representations [13]–[15], while degradation, survival, and availability models—together with EVT-based anomaly detectors—provide tools for threshold setting, timing metrics, and economic assessment [16], [17], [42]–[46], [49], [50]. However, these strands are often only loosely coupled in practice: deep PHM models typically optimize static classification metrics without exposing explicit control over alarm intensity or time-to-detect; EVT studies focus on score thresholding without survival-aware evaluation; and availability or ROI analyses are frequently applied downstream of heuristic alarm logic. A unified *online* framework that brings representation learning, calibrated decision rules, and survival-aware evaluation together is still lacking.

In this paper, we propose such an early-warning framework for rotating machinery. At a high level, the framework (i) controls false-alarm intensity by modeling healthy-score tails via extreme value theory (EVT), (ii) treats fault detection as a censorable time-to-event outcome summarized with survival analysis, and (iii) links detection and nuisance behavior to availability and return-on-investment (ROI) through established economic models [42]–[46], [49], [50]. As one compact instantiation of the representation layer, we employ a physics-guided tri-branch encoder, the Physics-Guided Tiny-Mamba Transformer (PG-TMT), which combines convolutional, state-space, and local-attention branches and aligns its attention with analytical order bands derived from bearing geometry. Decision outputs are produced by an EVT-calibrated on-threshold that targets a desired false-alarm intensity (events/hour), together with a dual-threshold hysteresis mechanism that stabi-

lizes episode-level alarms in streaming operation.

We evaluate the framework under a leakage-free *streaming* protocol with sliding windows, batch size one, and healthy-only calibration shared across all methods. Imbalance-aware accuracy (PR-AUC, ROC-AUC) is reported alongside censoring-aware timeliness (mean time-to-detect at matched intensity), Numenta-style early-warning scores, and calibration measures; robustness is probed through noise and domain/sensor-shift experiments on CWRU, Paderborn, XJTU-SY, and an industrial pilot [22]–[25].

The main contributions are threefold. (1) We formulate an early-warning framework that unifies EVT-based false-alarm intensity control, survival-based timing metrics, and availability/ROI modeling for *online* condition monitoring. (2) We design PG-TMT, a compact physics-guided encoder with order-band-aligned attention, providing interpretable evidence suitable for edge deployment. (3) We provide extensive leakage-safe streaming evaluation on public benchmarks and an industrial pilot, showing improved PR-AUC and reduced time-to-detect at matched intensity, and we release split manifests, code, and deployment artifacts to facilitate reproducible reliability studies.

II. METHOD: PHYSICS-GUIDED TINY-MAMBA TRANSFORMER

PG-TMT is a compact, physics-aware encoder for *online* early warning under class imbalance and domain shift. It combines: (i) a three-branch sequence encoder that captures complementary temporal–spectral cues, (ii) vibration priors derived from bearing physics, and (iii) a statistically principled decision layer with hysteresis. For a C -channel window $\mathbf{x}_t \in \mathbb{R}^{C \times L}$ with hop $h \ll L$ in streaming, the model outputs an anomaly score $s_t \in [0, 1]$ that is converted to online alarms via EVT-calibrated thresholds and hysteresis.

A. Architectural Overview

Stem + two sequence branches. A depthwise–separable 1-D convolutional stem extracts localized micro-transients; a Tiny–Mamba state-space branch models near-linear long-horizon dynamics; and a lightweight local-window Transformer encodes cross-channel coupling. Their outputs are fused to produce association–discrepancy evidence e_t and a calibrated score s_t (Fig. 1); the score is then mapped to streaming alarms by the EVT-based decision layer with hysteresis in Sec. II-C.

1) Convolution stem (micro-transients). A short stack of depthwise–pointwise blocks (with causal padding and optional dilation) preserves temporal resolution and outputs $\mathbf{y}_t^{\text{conv}} \in \mathbb{R}^{d_c}$, emphasizing impact-like transients.

2) Tiny–Mamba SSM branch (long-horizon trends). Selective/structured SSM layers capture slow degradation with stable recurrence:

$$\mathbf{h}_{t+1} = \mathbf{A}(\mathbf{g}_t) \mathbf{h}_t + \mathbf{B}(\mathbf{g}_t) \mathbf{u}_t, \quad (1)$$

$$\mathbf{y}_t^{\text{ssm}} = \mathbf{C} \mathbf{h}_t, \quad (2)$$

where \mathbf{u}_t is a channel-reduced input, $\mathbf{h}_t \in \mathbb{R}^{d_{\text{ssm}}}$ is the latent state, and gates \mathbf{g}_t modulate low-rank/diagonal ($\mathbf{A}, \mathbf{B}, \mathbf{C}$).

Stability parameterization. To ensure $\rho(\mathbf{A}) < 1$, we parameterize a continuous-time diagonal $\mathbf{A}_c = -\text{softplus}(\boldsymbol{\eta})$ and use zero-order-hold discretization:

$$\mathbf{A} = \exp(\Delta \mathbf{A}_c), \quad \mathbf{B} = \left(\int_0^\Delta \exp(\tau \mathbf{A}_c) d\tau \right) \mathbf{B}_c,$$

so that $\Re(\lambda(\mathbf{A}_c)) < 0 \Rightarrow \rho(\mathbf{A}) < 1$ and recurrent dynamics remain stable.

3) Lightweight Transformer branch (cross-channel couplings). With causal neighborhood $\mathcal{N}_W(t) = \{i \mid t - W \leq i \leq t\}$ and N_h heads, per-head attention is

$$\alpha_{t,i}^{(h)} = \frac{\exp(\langle \mathbf{q}_t^{(h)}, \mathbf{k}_i^{(h)} \rangle / \sqrt{d_{\text{head}}})}{\sum_{j \in \mathcal{N}_W(t)} \exp(\langle \mathbf{q}_t^{(h)}, \mathbf{k}_j^{(h)} \rangle / \sqrt{d_{\text{head}}})}, \quad i \in \mathcal{N}_W(t), \quad (3)$$

yielding $\mathbf{y}_t^{\text{att}} \in \mathbb{R}^{d_a}$ that summarizes local cross-channel structure.

4) Fusion and association–discrepancy evidence. We fuse $\mathbf{z}_t = [\mathbf{y}_t^{\text{conv}} \parallel \mathbf{y}_t^{\text{ssm}} \parallel \mathbf{y}_t^{\text{att}}]$ using a gated residual:

$$\boldsymbol{\gamma}_t = \sigma(\mathbf{W}_\gamma \mathbf{z}_t), \quad (4)$$

$$\mathbf{r}_t = \boldsymbol{\gamma}_t \odot (\mathbf{W}_f \mathbf{z}_t) + (\mathbf{1} - \boldsymbol{\gamma}_t) \odot \mathbf{z}_t. \quad (5)$$

Aggregating (3) across heads yields a local association over time:

$$p_t(i) = \frac{1}{N_h} \sum_{h=1}^{N_h} \alpha_{t,i}^{(h)}, \quad \sum_{i \in \mathcal{N}_W(t)} p_t(i) = 1. \quad (6)$$

To ensure numerical stability in divergences, we smooth p_t and a slow prior \tilde{p}_t (e.g., an EMA of past p) with the uniform u_t on $\mathcal{N}_W(t)$:

$$\bar{p}_t = (1 - \varepsilon)p_t + \varepsilon u_t, \quad \tilde{p}_t = (1 - \varepsilon)\tilde{p}_t + \varepsilon u_t, \quad \varepsilon \in (0, 0.5). \quad (7)$$

We then define the Jensen–Shannon discrepancy and evidence:

$$\text{disc}(p_t, \tilde{p}_t) = \frac{1}{2} \text{KL}(\bar{p}_t \parallel m_t) + \frac{1}{2} \text{KL}(\tilde{p}_t \parallel m_t), \quad (8)$$

$$m_t = \frac{1}{2}(\bar{p}_t + \tilde{p}_t), \quad 0 \leq \text{disc} \leq \log 2, \quad (9)$$

$$e_t = \mathbf{w}^\top \mathbf{r}_t + \lambda_{\text{disc}} \cdot \text{disc}(p_t, \tilde{p}_t), \quad (10)$$

$$s_t = \phi(e_t), \quad \phi(e) = \sigma(\kappa e + \beta), \quad \kappa > 0. \quad (11)$$

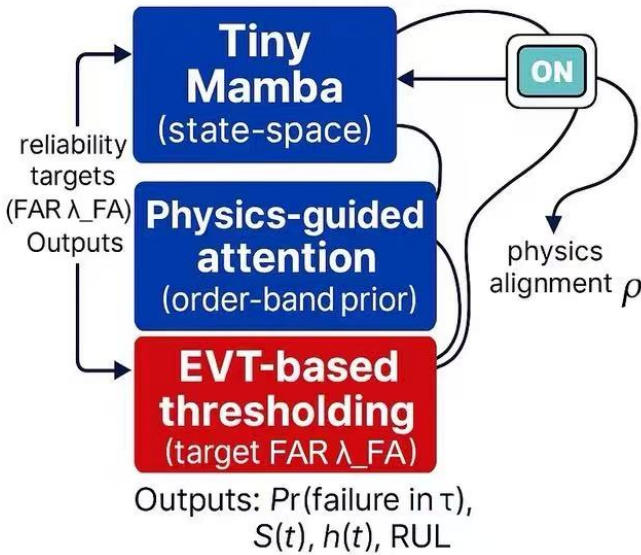
a) Calibration (post hoc).: ϕ is a scalar, monotone calibrator acting on the evidence e_t . In practice we use temperature scaling (learn κ on held-out healthy/near-healthy data; set $\beta = 0$) or isotonic regression under strong class imbalance to improve probability calibration without changing the ranking, thereby preserving the EVT tail fit and operating point.

B. Physics-Guided Priors

We bias learning toward physically admissible manifolds while preserving data fit, so that attention aligns with resonance belts and order harmonics. Fig. 2 visualizes physics-learning agreement; Table I summarizes priors and decision rules.

Reliability-calibrated online condition monitoring with a physics-guided tiny state-space model

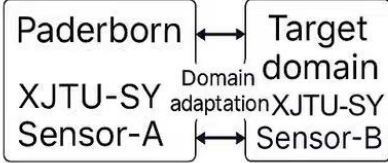
(A) Architecture & Reliability Loop



(B) Online condition (stateful)

Hysteresis (on/off) + cooldown

(D) Distribution-shift robustness



(C) Physics alignment & interpretability

Higher $ρ$ -lower FAR, higher POD

Band-alignment score

Fig. 1. PG-TMT overview. A Tiny-Mamba state-space branch, a compact Transformer (cross-channel couplings), and a convolutional stem are fused. The fusion output r_t and association p_t produce a calibrated score s_t , which is converted to online alarms via the EVT-based decision layer with hysteresis.

A. MSD residual regularization: Assuming a lumped mass-spring-damper surrogate $m\ddot{y} + c\dot{y} + ky = f(t) + \varepsilon(t)$,

$$r(t) = m\ddot{y} + c\dot{y} + ky - f(t), \quad \mathcal{L}_{\text{msd}} = \lambda_{\text{msd}} \|r\|_2^2. \quad (12)$$

Discretization. With sampling rate F_s , we use backward differences $\dot{y} \approx F_s (y_n - y_{n-1})$, $\ddot{y} \approx F_s^2 (y_n - 2y_{n-1} + y_{n-2})$; k, c may be constant or slowly varying via an SSM readout.

B. Temporal attention \rightarrow spectral attention (closed form): Let F_s and grid $\{f_k\}_{k=0}^{N_f-1} \subset [0, F_s/2]$. We project p_t to frequency by the normalized squared magnitude of a weighted DFT:

$$\tilde{A}_t(f_k) = \left| \sum_{i \in \mathcal{N}_W(t)} p_t(i) e^{-j2\pi f_k(i-i_0)/F_s} \right|^2, \quad (13)$$

where i_0 denotes the center index of $\mathcal{N}_W(t)$.

$$A_t(f_k) = \frac{\tilde{A}_t(f_k)}{\sum_k \tilde{A}_t(f_k)}. \quad (14)$$

Remark. This can be implemented via FFT with weights $p_t(i)$ at $O(W \log W)$ cost per step.

C. Physics-derived band mask: Given geometry $\{N_b, d, D_p, \theta\}$ and rotation f_r (Hz estimate $f_r = \hat{\Omega}/(2\pi)$;

rpm $n = 60 f_r$), we define classical fault orders:

$$\text{BPFI} = \frac{N_b}{2} f_r \left(1 + \frac{d}{D_p} \cos \theta \right), \quad (15)$$

$$\text{BPFO} = \frac{N_b}{2} f_r \left(1 - \frac{d}{D_p} \cos \theta \right), \quad (16)$$

$$\text{BSF} = \frac{D_p}{2d} f_r \left[1 - \left(\frac{d}{D_p} \cos \theta \right)^2 \right], \quad (17)$$

$$\text{FTF} = \frac{1}{2} f_r \left(1 - \frac{d}{D_p} \cos \theta \right). \quad (18)$$

With sidebands $f_{j,m} = f_j + m f_r$ ($m = -K_s \dots K_s$), we define a Gaussian-mixture mask

$$M_t(f_\ell) \propto \sum_{j \in \mathcal{J}} \sum_{m=-K_s}^{K_s} w_{j,m} \exp \left(-\frac{(f_\ell - f_{j,m})^2}{2\sigma_j^2} \right), \quad (19)$$

$$\sum_\ell M_t(f_\ell) = 1. \quad (20)$$

D. Spectral alignment loss: To avoid singularities, we smooth with uniform u_f :

$$\bar{A}_t = (1 - \zeta) A_t + \zeta u_f, \quad (21)$$

$$\bar{M}_t = (1 - \zeta) M_t + \zeta u_f, \quad \zeta \in (0, 0.5). \quad (22)$$

We then match distributions and penalize roughness:

$$\mathcal{L}_{\text{align}} = \lambda_{\text{align}} \text{KL}(\bar{M}_t \| \bar{A}_t) + \lambda_{\text{lap}} \sum_{k=0}^{N_f-1} |(\nabla_f \bar{A}_t)(f_k)|. \quad (23)$$

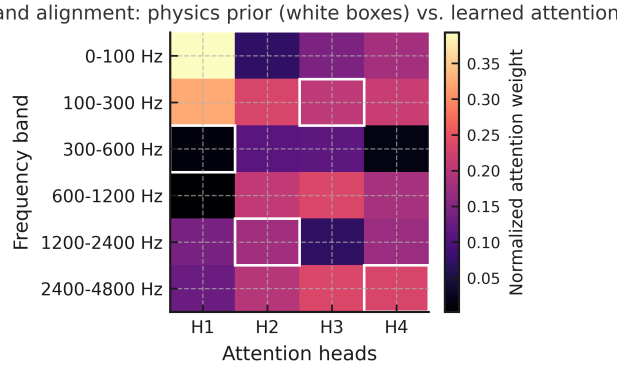


Fig. 2. Physics–learning alignment. Heat shows agreement between $M_t(f)$ and the learned $A_t(f)$; bright bands near BPFI/BPFO/BSF/FTF (and sidebands) indicate physically meaningful focus.

Since A_t is the weighted-DFT image of p_t by (13), minimizing (23) biases *temporal* attention toward admissible orders. The total physics prior is

$$\mathcal{L}_{\text{phys}} = \mathcal{L}_{\text{msd}} + \mathcal{L}_{\text{align}}. \quad (24)$$

To summarize physics–learning agreement over runs, we also track a simple band-alignment score $\rho \in [0, 1]$ that measures the normalized overlap between $A_t(f)$ and $M_t(f)$ (higher ρ indicates that attention concentrates within the analytical order bands). In the ablations of Sec. V (Table II), removing physics-guided priors consistently reduces ρ and increases the realized false-alarm intensity at a given target λ_{FA} , providing quantitative evidence that spectral alignment improves both physical plausibility and the stability of early-warning decisions.

C. Decision Layer: EVT-Based Thresholding and Hysteresis

Notation (avoid overload). Let λ_{FA} denote the *target false-alarm intensity* (episodes/hour), i.e., the acceptable rate of nuisance alarm *episodes* agreed with practitioners (e.g., “no more than a few false episodes per week”). To avoid overloading the calibrator slope in (11), we denote it by κ and write $\phi(e) = \sigma(\kappa e + \beta)$ throughout.

1) Peaks-over-threshold (POT) modeling and target intensity. We explain how raw anomaly scores are turned into an operating point that attains a prescribed λ_{FA} . On healthy calibration segments, we focus on the *tail* of the score distribution and model exceedances of s_t above a high level u . Under the peaks-over-threshold (POT) setting, the conditional excess

$$Y = s_t - u \mid s_t > u$$

follows a generalized Pareto distribution $\text{GPD}(\xi, \beta)$, and exceedance arrivals above u form (to first order) a Poisson process with rate λ_u (episodes/hour). Intuitively, u is chosen as a high quantile of healthy scores (e.g., between the 95th and 99th percentile), so that only rare, extreme fluctuations are modeled; the corresponding rate λ_u summarizes how often such extremes occur per hour under normal operation.

For any candidate decision threshold $\tau \geq u$,

$$\Pr(s_t > \tau \mid s_t > u) = (1 + \xi(\tau - u)/\beta)_+^{-1/\xi},$$

so the unconditional exceedance intensity above τ is

$$\lambda_\tau = \lambda_u \Pr(s_t > \tau \mid s_t > u).$$

Proposition (closed-form on-threshold). The on-threshold that attains the target intensity λ_{FA} solves $\lambda_\tau = \lambda_{\text{FA}}$ and satisfies

$$\tau_{\text{on}} = u + \frac{\beta}{\xi} \left[\left(\frac{\lambda_u}{\lambda_{\text{FA}}} \right)^\xi - 1 \right], \quad \lim_{\xi \rightarrow 0} \tau_{\text{on}} = u + \beta \ln \left(\frac{\lambda_u}{\lambda_{\text{FA}}} \right). \quad (25)$$

Validity domain: $0 < \lambda_{\text{FA}} \leq \lambda_u$ and $1 + \xi(\tau_{\text{on}} - u)/\beta > 0$ (if $\xi < 0$ then $\tau_{\text{on}} \leq u - \beta/\xi$). **Proof sketch.** Substitute $\lambda_\tau = \lambda_u (1 + \xi(\tau - u)/\beta)^{-1/\xi}$, set $\lambda_\tau = \lambda_{\text{FA}}$, and rearrange.

In practice, we estimate (ξ, β, λ_u) on healthy-only calibration data, set u to a high quantile of the score distribution, and compute τ_{on} from (25). The target intensity λ_{FA} then serves as a practitioner-facing control (“acceptable nuisance episodes per hour”).

2) Dual thresholds, hold time, and alarm episodes (hysteresis).

The EVT mapping above specifies *when* scores are high enough to trigger an alarm, but does not prevent rapid on/off chatter. For deployment, operators care about the rate of *alarm episodes* rather than isolated frame-level toggles. We therefore define a simple hysteresis rule with dual thresholds and a minimum hold time:

$$\text{ALARM}_t = \begin{cases} 1, & s_t \geq \tau_{\text{on}}, \\ 0, & s_t \leq \tau_{\text{off}} := \tau_{\text{on}} - \delta \\ & \text{and } t - t_{\text{on}} \geq T_{\min}, \\ \text{ALARM}_{t-1}, & \text{otherwise,} \end{cases}$$

where $\delta > 0$ creates an off-gap and $T_{\min} > 0$ enforces a minimum episode length; t_{on} denotes the most recent onset time. An *alarm episode* is a maximal contiguous run of $\text{ALARM}_t = 1$ values, separated from the next by at least one time point with $\text{ALARM}_t = 0$. To further avoid fragmentation of near-adjacent alarms, we apply a short refractory or merging interval ΔT_{merge} in post-processing: episodes whose gaps are shorter than ΔT_{merge} are merged into a single event. The empirical false-alarm intensity λ_{FA} is then computed as the number of alarm episodes per hour of *healthy* data under this rule, so that FAR is directly interpreted as an estimate of λ_{FA} .

RPM-aware adaptation. Under speed drift, the score distribution and thus the effective EVT tail can vary with shaft speed $\hat{\Omega}(t)$. To stabilize the achieved intensity, we allow τ_{on} to depend weakly on speed via a slow map $\hat{\Omega}(t) \mapsto \tau_{\text{on}}(\hat{\Omega}(t))$ (e.g., a piecewise log-linear fit of τ_{on} against $\hat{\Omega}$ learned from healthy data). This preserves the target λ_{FA} in the presence of order shifts, while the hysteresis and merging rules above keep the notion of an alarm episode consistent across operating regimes. Empirically, after binning by rpm and calibrating within each bin, the realized false-alarm intensity $\hat{\lambda}_{\text{FA}}$ fluctuates within a narrow band around the target across speed regimes, consistent with the stable FAR trends in Fig. 5d.

D. Learning Objective and Calibration

Task loss under imbalance. Given binary labels $y_t \in \{0, 1\}$ on curated datasets, we employ either class-balanced BCE or focal loss to account for severe rarity of faults.

Total objective.

$$\mathcal{L} = \mathcal{L}_{\text{task}} + \mathcal{L}_{\text{phys}}. \quad (26)$$

When labels are unavailable (e.g., cold start), $\mathcal{L}_{\text{task}}$ can be replaced by a one-class/self-supervised proxy (e.g., reconstruction or contrastive) while keeping $\mathcal{L}_{\text{phys}}$ unchanged, so that physics priors remain active.

E. Complexity-Aware Design and Streaming Inference

Per-step computational cost. Depthwise convolution costs $O(C L k)$, the SSM update $O(d_{\text{ssm}})$, local attention $O(N_h W d_{\text{head}})$, and spectral alignment (FFT) $O(W \log W)$ (with optional downsampling).

Stateful streaming. We cache $(\mathbf{h}_t, \mathbf{K}, \mathbf{V})$ and slide with hop $h \ll L$ to avoid redundant computation, tightening p_{90}/p_{99} latency tails and enabling stable real-time operation.

Tooling. We export models to ONNX/TensorRT with `batch=1`; FP16 kernels yield substantial throughput gains with negligible impact on PR-AUC or MTTD.

III. DATASETS AND EVALUATION PROTOCOLS

We describe datasets, leakage-safe splits, streaming setup, noise, threshold calibration, and metrics for *online* evaluation. Protocols are designed to (i) prevent train–test leakage, (ii) reflect on-device streaming with `batch=1`, and (iii) yield reliability-centered metrics. Unless otherwise noted, *all methods* share the same windowing, calibration (EVT + hysteresis), and evaluation code so that comparisons are made at *matched* alarm intensity rather than at heuristic thresholds.

A. Datasets and Leakage Control

CWRU (motor-bearing rig). Multiple loads, speeds, rigs, and sampling regimes. Splits ensure that no (*machine, load, speed, sampling*) tuple appears in more than one split [22], [23].

Paderborn (seeded faults). Speed×torque grids and heterogeneous drive trains. Source→target transfers differ by *at least one* axis (load/speed) and/or sensor/rig [24].

XJTU-SY (run-to-failure). Chronological splits: early healthy segments are used for training/calibration; subsequent stages are reserved for *early-warning* tests [25].

Leakage control (all datasets).: (i) Splits are defined at the *machine/rig* level with disjoint operating-point tuples; (ii) overlapping windows never cross split boundaries; (iii) if resampling is needed, the target rate and filters are chosen *within* each split; (iv) per-channel normalization uses *train-only* statistics; (v) EVT tail calibration (Sec. III-E) uses *healthy or near-healthy* windows preceding the test horizon; (vi) all ablations and baselines reuse the same split manifests and preprocessing code.

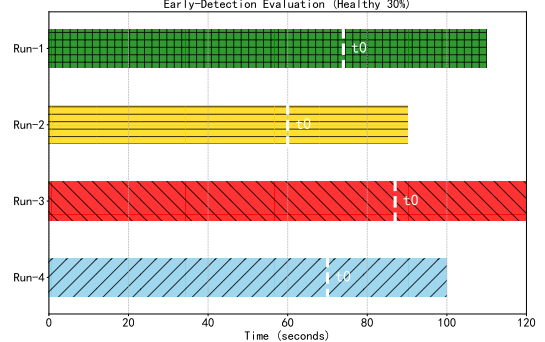


Fig. 3. Streaming timeline. t_{phys} : first physically detectable deviation (label or expert annotation); t_0 : first issued decision under hysteresis (Sec. III-E). Windows contributing to MTTD/FAR/PR-AUC are highlighted. A refractory interval ΔT_{merge} merges nearby onsets; runs with no alarm by horizon end are right-censored.

B. Windows, Cold Start, and Streaming Setup

Sliding windows of length L and hop $h \ll L$ emulate *online* condition monitoring. A burn-in period of T_{burn} windows initializes SSM states and attention KV caches and collects healthy/near-healthy statistics for calibration; detections during burn-in are ignored. Thereafter, streaming inference runs at `batch=1` with state caching and fixed hop.

Reference times (Fig. 3).: For each run r , $t_{\text{phys}}^{(r)}$ is the first physically detectable deviation and $t_0^{(r)}$ is the first alarm time under the dual-threshold policy. Runs with no alarm by horizon end are *right-censored*. MTTD aggregates $\Delta^{(r)} = t_0^{(r)} - t_{\text{phys}}^{(r)}$ across runs with censoring-aware estimators (below).

C. Domain-Shift Tasks (Cross-Load/Speed/Sensor/Machine)

We evaluate three shift families: (i) cross-load/speed within a dataset; (ii) cross-sensor/rig; and (iii) cross-dataset (e.g., CWRU→Paderborn, Paderborn→XJTU-SY). Each directed task reports source-only, post-adaptation, and retention (accuracy and timeliness), following PHM transfer-learning practice [26]–[28], [33], [34]. Retention and gain are computed at *matched* false-alarm intensity to avoid threshold confounding.

D. Noise Model and SNR Setting

To probe robustness, we add zero-mean white noise to reach $\text{SNR} \in \{0, 5, 10, 15, 20\}$ dB. For $\mathbf{x} \in \mathbb{R}^{C \times L}$ with per-sample, per-channel average power $\|\mathbf{x}\|_F^2 / (CL)$,

$$\text{SNR}_{\text{dB}} = 10 \log_{10} \left(\frac{\|\mathbf{x}\|_F^2 / (CL)}{\sigma_n^2} \right),$$

so we set $\sigma_n^2 = (\|\mathbf{x}\|_F^2 / (CL)) \cdot 10^{-\text{SNR}_{\text{dB}}/10}$ per window. Noise is injected *after* training-set normalization; unless stated, channels receive independent draws.

E. Threshold Calibration and Hysteresis

Thresholds are calibrated on healthy/near-healthy windows via EVT. Let u be a high preliminary level; exceedances $Y = s_t - u \mid s_t > u$ follow a GPD(ξ, β) and exceedance arrivals above u are modeled as a Poisson process with rate

TABLE I
SUMMARY OF PHYSICS-GUIDED PRIORS AND DECISION LAYER

Component	Purpose	Eq.	Key hyperparameters
MSD residual \mathcal{L}_{msd}	Trajectory consistency; enables tracking of $\hat{k}(t), \hat{c}(t)$	(12)	λ_{msd} ; (m, k, c) / SSM readout
Spectral alignment $\mathcal{L}_{\text{align}}$	Match $A_t(f)$ to $M_t(f)$; suppress non-physical peaks	(13), (19), (23)	$\lambda_{\text{align}}, \lambda_{\text{lap}}, N_f, K_s, \{\sigma_j, w_{j,m}\}, \hat{\Omega}(t)$
EVT thresholding (GPD)	Calibrate τ_{on} to target false-alarm intensity (events/hour)	(25)	$(u, \xi, \beta); \lambda_u; \lambda_{\text{FA}}$
Hysteresis + hold time	Stabilize streaming alarms; reduce chatter/fragmentation	—	$\tau_{\text{off}} = \tau_{\text{on}} - \delta; T_{\text{min}}; \Delta T_{\text{merge}}$
Task loss $\mathcal{L}_{\text{task}}$	Handle imbalance; learn decision-relevant score s_t	—	w_+, w_- (or focal γ)

λ_u (episodes/hour). For a target false-alarm intensity λ_{FA} (episodes/hour), the *on*-threshold is

$$\tau_{\text{on}} = u + \frac{\beta}{\xi} \left[\left(\frac{\lambda_u}{\lambda_{\text{FA}}} \right)^\xi - 1 \right], \quad \lim_{\xi \rightarrow 0} \tau_{\text{on}} = u + \beta \ln \frac{\lambda_u}{\lambda_{\text{FA}}}.$$

This expression is valid when $0 < \lambda_{\text{FA}} \leq \lambda_u$ and $1 + \xi(\tau_{\text{on}} - u)/\beta > 0$. We apply $\tau_{\text{off}} = \tau_{\text{on}} - \delta$ with $\delta > 0$ and a minimum hold time T_{min} to implement hysteresis. In practice, u is chosen as a high quantile (e.g., 95–99%) of healthy scores with sufficient exceedances; (ξ, β) and λ_u are estimated on the calibration segment. For speed drift, we optionally maintain $\tau_{\text{on}}(\hat{\Omega})$ across rpm bins. *Applying the refractory interval ΔT_{merge} is equivalent to declustering of extreme scores, improving the validity of the Poisson-arrival assumption in EVT.*

F. Primary Metrics

PR-AUC and ROC-AUC. We report both, emphasizing PR-AUC under class imbalance [18]. Scores s_t are evaluated over streaming windows; operating points for timing metrics are taken at *matched* alarm intensity.

MTTD (lead time). For run r , $\Delta^{(r)} = t_0^{(r)} - t_{\text{phys}}^{(r)}$. Because misses induce right censoring, we summarize $\{\Delta^{(r)}\}$ via Kaplan–Meier curves and report mean/median lead time with confidence intervals; group comparisons may use Cox proportional-hazards models (hazard ratios) [36], [37].

False-alarm intensity (FAR). Episodes are formed by applying hysteresis and then merging onsets closer than a refractory interval ΔT_{merge} ; FAR is the number of unique episodes per hour on *healthy* data. We denote the target intensity by λ_{FA} and its empirical estimate by $\hat{\lambda}_{\text{FA}}$.

Latency. Per-window inference with `batch=1` after warm-up; we report p50/p90/p99 and sustainable FPS on CPU/Jetson. All latencies include pre-/post-processing and EVT evaluation.

Calibration and significance. Reliability diagrams and expected calibration error (ECE) quantify probability calibration; DeLong’s test compares AUCs; multiple comparisons use Benjamini–Hochberg FDR control [38]–[40]. Where applicable, NAB-style scoring complements timeliness and nuisance-cost reporting [19].

G. Validation Protocol and Confidence Intervals

Hyperparameters are tuned on a *machine/rig-level* validation split to prevent leakage. Each configuration is repeated with multiple seeds; unless noted, all methods share the same windowing, calibration, and evaluation code. We report mean \pm 95% confidence intervals over runs/seeds; PR-AUC

and MTTD intervals are bootstrapped at the run level. For AUC comparisons, p -values come from DeLong’s test with BH–FDR correction; for timing comparisons, we complement summary statistics with KM curves and Cox hazard ratios.

H. Reproducibility Artifacts

We release preprocessing scripts, split manifests, and configuration files for *online* evaluation (including EVT and refractory parameters), together with ONNX/TensorRT exporters and latency/FPS harnesses. Commit hashes, seed files, and environment manifests are provided to support exact replication of figures and tables (Sections IV and VI).

IV. ONLINE EARLY-WARNING RESULTS

We evaluate PG-TMT under the streaming protocol in Section III with `batch=1`. We focus on: (i) latency distributions and sustainable FPS (Fig. 4, Table III); (ii) robustness to additive noise across SNR sweeps (Fig. 5, Tables IV–V); and (iii) qualitative early-warning behavior along the timeline in Fig. 3. Metrics follow imbalance-aware practice [18], [19]; operating thresholds use EVT with hysteresis [16], [17] at matched false-alarm intensity.

A. Latency Distributions and Throughput (`batch=1`)

PG-TMT yields tight latency CDFs with narrow high-percentile tails on desktop CPU and embedded Jetson, consistent with stateful Tiny–Mamba updates, attention KV caching, and depthwise–separable convolutions. Across window sizes, sustainable FPS exceeds dataset acquisition rates, leaving headroom for on-device EVT and logging (Fig. 4). End-to-end percentiles, FLOPs, and parameter budgets appear in Table III.

B. Robustness to Additive Noise

With thresholds calibrated at a high-SNR reference and held fixed across SNR sweeps (e.g., 20 dB in Fig. 5d), three observations are consistent across CWRU, Paderborn, and XJTU-SY (Fig. 5; Tables IV–V): (i) PR-AUC degrades gracefully as SNR drops, reflecting complementary cues from the convolutional stem and the SSM branch; (ii) MTTD increases moderately at low SNR but remains competitive as band-aligned attention stabilizes defect orders; (iii) FAR remains contained via EVT plus hysteresis, which suppresses short-lived excursions.

Note. Cross-domain/sensor transfer results are provided in Section V and Fig. 6 under matched-intensity evaluation with EVT thresholds and hysteresis.

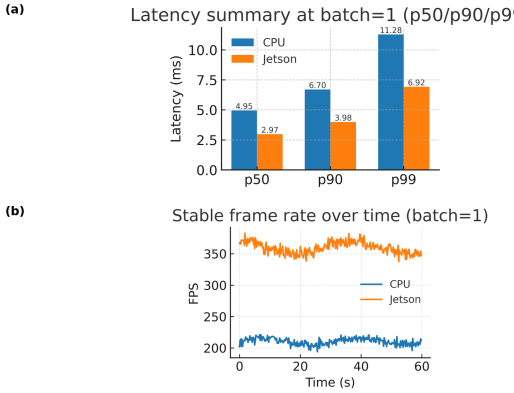


Fig. 4. Deployment metrics at $\text{batch}=1$. (a) p50/p90/p99 latency on CPU and Jetson. (b) Sustainable frame rate over time. Narrow tails indicate predictable real-time behavior suitable for on-device EVT and logging.

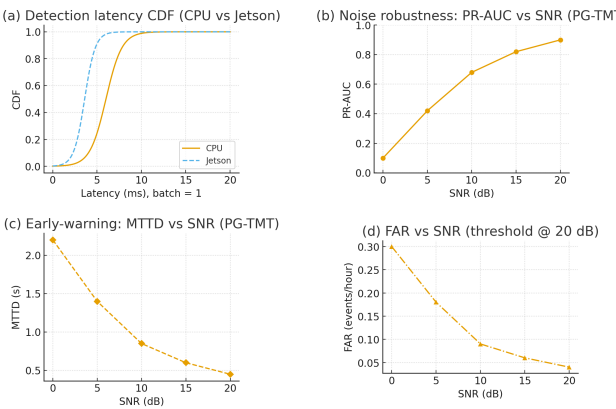


Fig. 5. Noise robustness. (a) Latency CDF (CPU vs. Jetson) at $\text{batch}=1$. (b) PR-AUC vs. SNR. (c) MTTD vs. SNR. (d) FAR vs. SNR (threshold calibrated at a high-SNR reference). Curves are aggregated across datasets under the protocol in Section III.

C. Alarm Stability with EVT and Hysteresis

On healthy/near-healthy windows we fit a GPD tail above a high reference u and set τ_{on} for a target false-alarm intensity; the off-threshold $\tau_{\text{off}} = \tau_{\text{on}} - \delta$ and a minimum hold time T_{min} implement hysteresis. With RPM-aware adaptation of τ_{on} , decision-time variance is reduced (cf. Fig. 5a), and the refractory merging in Section III prevents alarm fragmentation.

D. Qualitative Early-Warning Cases

On run-to-failure (XJTU-SY) and staged-fault (CWRU/Paderborn) sequences, PG-TMT triggers *earlier and stabler* episodes relative to the physical onset t_{phys} in Fig. 3: as attention concentrates near fault orders, the association-discrepancy score rises while the SSM state tracks slow stiffness/damping surrogates; EVT plus hysteresis converts these patterns into actionable alarms.

V. CROSS-DOMAIN/SENSOR ADAPTATION AND ABLATIONS

We assess transfer robustness under the leakage-safe protocol in Section III and isolate PG-TMT design factors via

ablations. Baselines include domain-adversarial and discrepancy methods [26]–[28] and strong supervised references [32]–[34]. *All models share identical preprocessing and decision pipelines* (windowing, EVT calibration, hysteresis); operating points are set at a *matched* false-alarm intensity (events/hour). On each target domain, τ_{on} is re-estimated from healthy windows to hold the same λ_{FA} (Section III-E).

A. Cross-Domain/Sensor Transfer

We consider three families of shift: (i) cross-load/speed *within* dataset; (ii) cross-sensor/rig; and (iii) cross-dataset (e.g., CWRU→Paderborn, Paderborn→XJTU-SY). Fig. 6 visualizes the directed task graph (left), AUC retention (middle), and MTTD retention/gain (right). Three observations consistently hold:

- **Cross-load/speed.** Band-aligned spectral attention stabilizes defect-order harmonics against rpm variation, yielding high AUC retention and modest MTTD drift.
- **Cross-sensor/rig.** The Tiny-Mamba branch preserves low-frequency degradation dynamics, while the convolutional stem enhances channel-local transients, improving robustness to sensor/fixtures changes.
- **Cross-dataset.** Unsupervised adaptation recovers most discriminative ability; with 1–5% few-shot labels on the target, performance approaches supervised oracles.

For statistical reporting, PR/ROC AUC differences use DeLong's test with BH-FDR control across tasks; censoring-aware lead-time comparisons are summarized by Kaplan–Meier curves and Cox hazard ratios (HRs).

B. Retention and Transfer-Gain Metrics

To ensure consistent directions for “higher is better”, we use:

$$\text{Retention}_{\text{AUC}} = \frac{\text{AUC}_t}{\text{AUC}_s}, \quad \text{Gain}_{\text{AUC}} = \text{AUC}_a - \text{AUC}_s, \quad (27)$$

$$\text{Retention}_{\text{MTTD}} = \frac{\text{MTTD}_s}{\text{MTTD}_t}, \quad \text{Gain}_{\text{MTTD}} = \text{MTTD}_s - \text{MTTD}_a. \quad (28)$$

Here, $\text{Retention}_{\text{AUC}} \approx 1$ and $\text{Retention}_{\text{MTTD}} \approx 1$ indicate preservation under shift; positive gains reflect benefits from adaptation. Lead-time differences are complemented by KM/Cox analyses (HR>1 indicates earlier detection vs. baseline at matched intensity).

C. Ablation and Confidence Analysis

All variants reuse the same splits, windowing, EVT calibration, and streaming evaluation. We ablate four architectural components and the decision layer:

- **No physics priors** ($\lambda_{\text{align}} = \lambda_{\text{msd}} = 0$): spectral attention leaks to non-resonant bands (PR-AUC \downarrow) and FAR rises under the same λ_{FA} due to spurious excursions.
- **No Mamba branch:** long-horizon degradation cues weaken, increasing variance of detection times (wider KM tails, HR closer to 1).

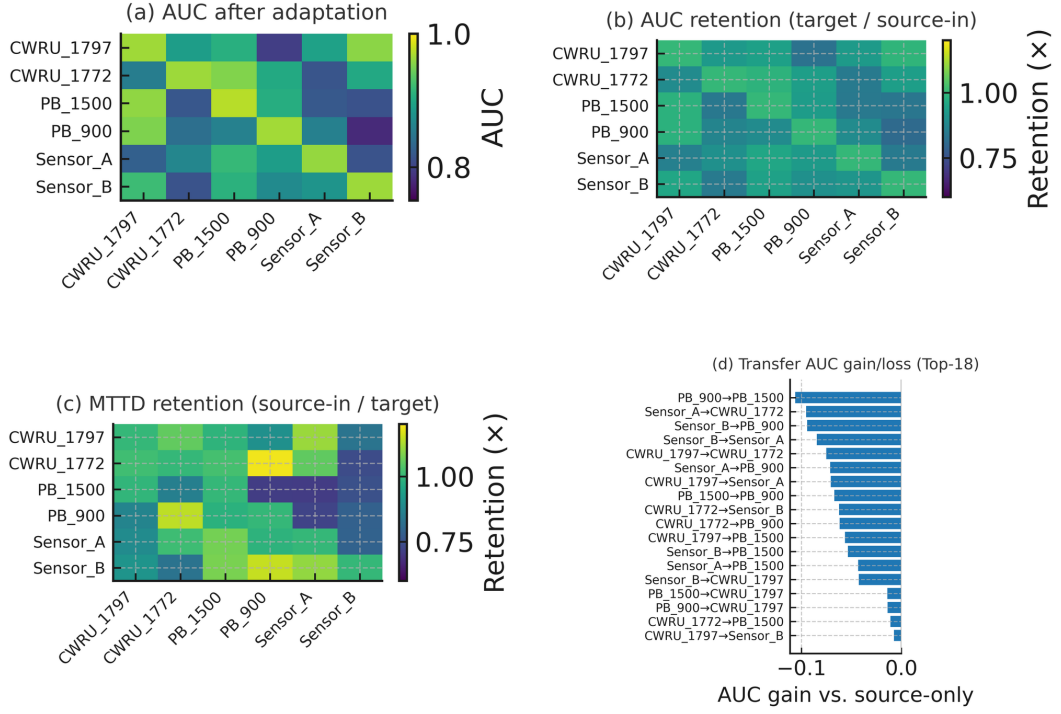


Fig. 6. Cross-domain/cross-sensor transfer. Left: directed task graph among CWRU, Paderborn, and XJTU-SY. Middle: AUC retention heat map (higher is better). Right: MTTD retention and transfer-gain bars at matched false-alarm intensity; positive gain indicates earlier detection on the target.

TABLE II
ABLATION DESIGN AND DIRECTIONAL IMPACT

Variant	Primary effect (qualitative)	Metrics (dir.)
No physics priors	Attention leaks beyond BPFI/BPFO/BSF/FTF	PR-AUC ↓, FAR ↑
No Mamba branch	Weaker long-horizon trend tracking	MTTD var. ↑, HR ↓
No Transformer	Cross-channel coupling under-modeled	AUC retention ↓
No conv stem	Transient sensitivity reduced	MTTD ↑
No hysteresis	Flickers not merged to episodes	FAR ↑
No EVT (fixed τ)	Intensity not matched across domains	Retention metrics biased

- **No Transformer branch:** cross-channel resonance is under-modeled, harming cross-sensor generalization (AUC retention \downarrow).
- **No convolutional stem:** sensitivity to micro-transients decreases, delaying onsets (MTTD \uparrow at matched intensity).
- **No hysteresis / no EVT:** removing hysteresis increases episode fragmentation (FAR \uparrow); using a fixed score threshold instead of EVT breaks intensity matching, confounding retention metrics.

Each configuration is repeated with multiple seeds; we report mean \pm 95% CIs via run-level bootstrap. Pairwise AUC differences vs. the full model use DeLong's test; MTTD curves are compared by log-rank with BH-FDR across datasets/tasks.

D. Efficiency–Accuracy Trade-offs

PG-TMT occupies a favorable Pareto frontier (Fig. 7), combining sub-1 MB parameters and sub-10 ms median end-to-end latency at batch= 1 (Table III) with strong PR-AUC under severe class imbalance [18]. For a given complexity or latency budget, it attains higher PR-AUC than the edge-class baselines; conversely, for comparable PR-AUC it requires fewer parameters and lower latency. Domain-adaptation variants reuse the same preprocessing and decision pipelines, so their inference latencies are those reported in Table III.

VI. INDUSTRIAL APPLICATION, DEPLOYMENT, AND REPRODUCIBILITY

We detail the end-to-end workflow, on-device runtime, pilot impact, and released artifacts in a reliability-centered style. Deployment assumes batch= 1 streaming with intensity-controlled decisions under class imbalance and physics-aligned evidence. Beyond the specific encoder (PG-TMT), the EVT-based intensity control, dual-threshold hysteresis, and the streaming evaluation protocol are *backbone-agnostic* and apply to any streaming anomaly score.

A. Pilot Scenario and Workflow Integration

Each machine train is instrumented with a multi-sensor vibration stack. Streaming windows run at batch= 1; the association-discrepancy score is converted to *episode-level* alarms using EVT with dual-threshold hysteresis (Section III-E) at a practitioner-specified false-alarm *intensity* (events/hour). RPM

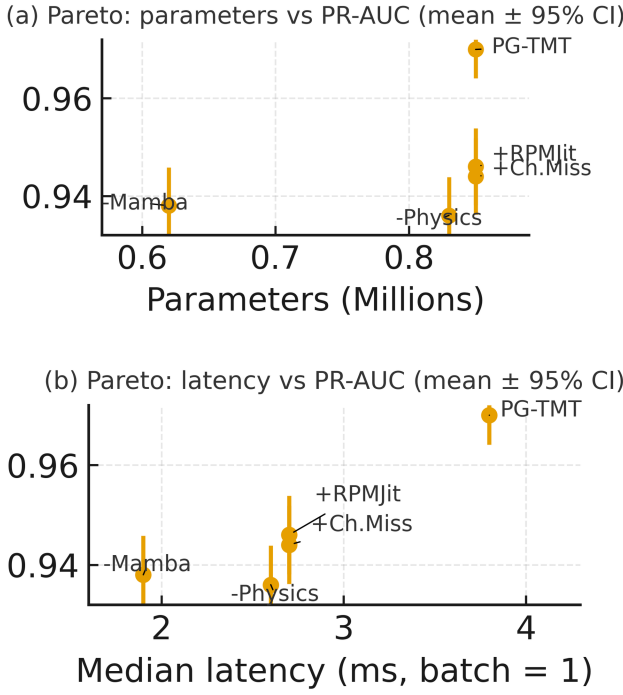


Fig. 7. Pareto trade-offs between model complexity/latency and imbalance-aware accuracy. Each point shows PR-AUC (mean \pm 95% confidence interval) versus parameter count and end-to-end latency at batch= 1. PG-TMT occupies a favorable frontier compared with edge-class baselines.

(order) estimates anchor spectral attention and enable mild RPM-aware adjustment of τ_{on} to stabilize sensitivity under operating-point drift. For triage and auditability, the UI surfaces physics-aligned attention (order-band focus), slow trend states from the SSM branch, and the score timeline as interpretable evidence panels. (Fig. 8) summarizes the field layout and end-to-end pipeline from sensing to CMMS integration.

B. On-Device Deployment and Runtime

Models are exported to ONNX and compiled with TensorRT; where available, fused depthwise/SSM kernels reduce tail latency. Latency percentiles and sustainable FPS (including pre-/post-processing and EVT evaluation) follow the streaming protocol in Section IV. On both CPU and Jetson, PG-TMT maintains sub-10 ms median (p_{50}) latency with narrow p_{90}/p_{99} , leaving headroom for on-device EVT, logging, and telemetry (Table III). For context, six edge-class backbones (DS-ConvNet-XS, Tiny-TCN-XS, LSTM-XS, ResNet1D-XS, SSM-Only, LocalAttn-Only) are evaluated under identical pre-processing and EVT pipelines; their end-to-end latencies are reported alongside.

C. Reliability and Business Impact

Earlier and stabler alarms—lower MTTD at *matched* false-alarm intensity and fewer nuisance episodes—translate into quantifiable availability gains and ROI. Standard PHM availability models convert (i) reduced mean downtime per episode and (ii) lower false-alarm handling burden into steady-state

availability improvements, while ROI analyses map these reliability gains to expected cost savings. In the pilot, RPM-aware compensation further suppresses false positives during speed transients. Accuracy under additive noise is summarized in Table IV; early-detection timeliness and false-alarm intensity appear in Table V, and the resulting downtime reduction is visualized in Fig. 9.

D. Reproducibility Package

We release machine/rig-level split manifests (CWRU, Paderborn, XJTU-SY), streaming evaluation scripts (windowing, cold start, NAB-style scoring, EVT utilities), PG-TMT checkpoints, ONNX exporters, TensorRT build specs, seed/config files for confidence intervals, and profiling harnesses aligned with Figs. 4 and 5. Commit hashes and environment manifests allow exact reproduction of all figures and tables.

E. Compliance With T-REL Expectations

The deployment satisfies key T-REL priorities: (i) batch=1 streaming with matched-intensity operation (Section III-E); (ii) robustness to noise and domain/sensor shift (Sections IV and V); (iii) physics-aligned interpretability (Fig. 2); and (iv) end-to-end reproducibility via released artifacts (Tables III–V).

VII. CONCLUSION

We presented the *Physics-Guided Tiny-Mamba Transformer* (PG-TMT) as an instance of a reliability-calibrated early-warning framework for *online* fault warning in rotating machinery. Instead of treating condition monitoring as a static imbalanced classification task, we cast streaming health assessment as a censorable time-to-event problem with an explicit trade-off between timeliness and false alarms. The framework couples a compact tri-branch encoder (depthwise-separable convolutions for impact-like micro-transients, a Tiny-Mamba state-space branch for long-horizon dynamics, and a local Transformer for cross-channel resonance [8]–[12]) with physics-guided priors that align temporal attention with *spectral* attention over analytical order bands (BPFI/BPFO/BSF/FTF [4]–[6]), and an EVT-based dual-threshold decision layer that exposes the target false-alarm intensity λ_{FA} (events/hour) as a practitioner-facing control while enforcing hysteresis for stable streaming alarms under severe class imbalance [16], [17]. Although instantiated with PG-TMT, the EVT calibration, time-to-event metrics, and availability/cost analyses are *backbone-agnostic* and can wrap any model that produces streaming anomaly scores.

Under a leakage-free streaming protocol emphasizing PR-AUC [18] and time-to-detection metrics, PG-TMT improves early-warning reliability and timeliness on CWRU, Paderborn, and XJTU-SY benchmarks [22]–[25]. At *matched* false-alarm intensity, the framework reduces mean time-to-detect and increases the probability of timely detection across operating conditions. Across SNR sweeps, PR-AUC degrades smoothly from clean/20 dB to 0 dB while mean time-to-detect remains on the order of tens of seconds and alarm intensity stays

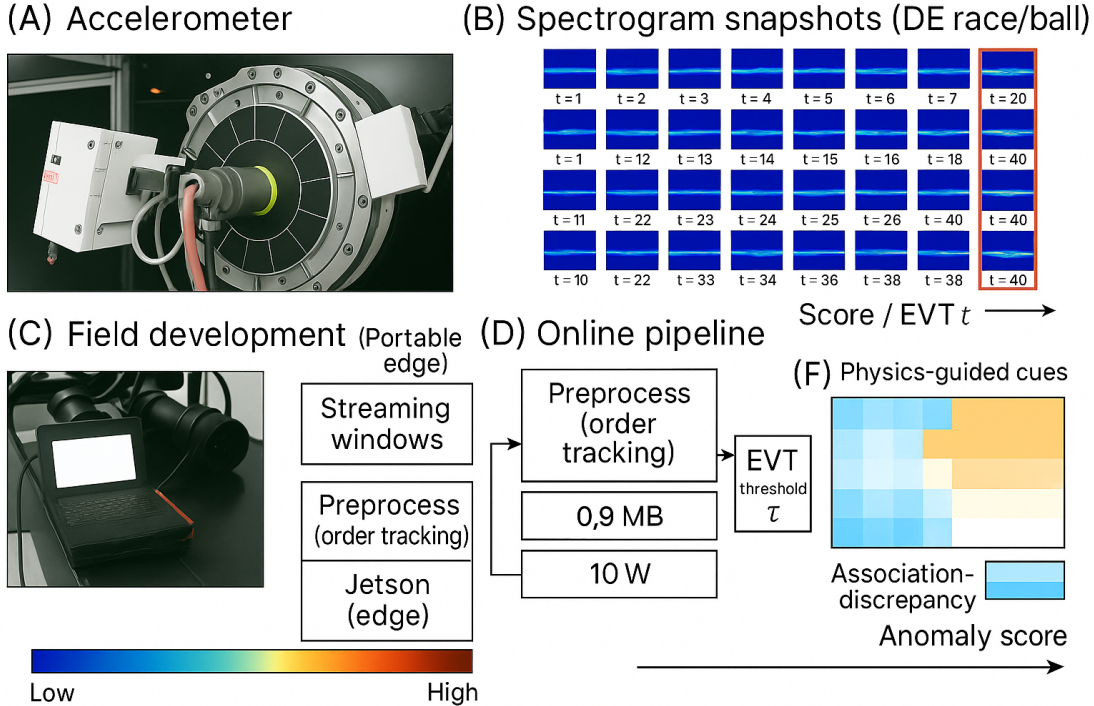


Fig. 8. Industrial workflow. Sensors feed streaming inference at $\text{batch}=1$ (Tiny-Mamba/Transformer branches with physics-aligned attention). EVT thresholding plus hysteresis yields intensity-controlled alarm *episodes*; RPM-aware compensation reduces nuisance during speed transients. Outputs (scores, episodes, and evidence panels) are logged and linked to CMMS for work order generation.

TABLE III
MODEL COMPLEXITY AND END-TO-END LATENCY AT BATCH=1 (INCLUDES PRE-/POST-PROCESSING AND EVT EVALUATION). PG-TMT ACHIEVES SUB-10 ms MEDIAN LATENCY WITH NARROW TAILS, WHEREAS SEVERAL BASELINES EXHIBIT HEAVIER p_{99} .

Model	Complexity		CPU latency (ms)			Jetson latency (ms)			Jetson FPS	Numeric precision
	Params (M)	FLOPs (G)	p_{50}	p_{90}	p_{99}	p_{50}	p_{90}	p_{99}		
PG-TMT (ours)	0.78	0.28	8.3	9.4	10.5	7.1	8.0	8.9	125	FP32 / FP16
DS-ConvNet-XS	0.60	0.24	8.2	10.8	13.9	7.0	9.3	12.8	120	FP32 / FP16
Tiny-TCN-XS	0.48	0.20	7.7	11.6	15.8	6.7	10.7	14.5	118	FP32 / FP16
LSTM-XS	0.41	0.19	8.9	12.7	16.3	7.6	11.2	14.9	112	FP32 / FP16
ResNet1D-XS	0.69	0.27	9.1	12.9	16.8	7.8	11.6	15.4	110	FP32 / FP16
SSM-Only (Mamba-XS)	0.42	0.17	7.9	10.3	13.2	6.8	9.1	12.1	121	FP32 / FP16
LocalAttn-Only (Transf-XS)	0.55	0.23	8.6	12.1	15.6	7.4	10.5	14.2	114	FP32 / FP16

per-window latency is measured after warm-up with a fixed hop h and batch=1. CPU runs use FP32; Jetson runs use FP16. Domain-adaptation variants reuse these backbones, so their latencies match the corresponding entries.

below one episode per hour, indicating operationally acceptable robustness. The complexity-aware design and streaming inference yield a favorable accuracy–efficiency Pareto front (sub-1 MB parameters; end-to-end latency ≤ 10 ms at $\text{batch}=1$), enabling on-device deployment on CPUs and embedded GPUs. Physics–learning alignment visualizations connect attentional evidence to measurable vibration modes, supporting threshold setting and root-cause analysis and making alarm logic more interpretable to domain experts.

An industrial pilot on a rotating machinery asset further demonstrates how the framework can be integrated into existing workflows, from sensor layout and on-device inference to EVT calibration and RPM-aware compensation. Combining improved timeliness and reduced nuisance alarms with standard availability and cost models associates the proposed

early-warning layer with higher steady-state availability and reduced expected downtime relative to incumbent monitoring logic. In this way, statistically grounded improvements in streaming detection are linked directly to maintenance planning and business impact, moving beyond offline accuracy gains toward reliability-centered asset management.

Limitations and future work. PG-TMT currently relies on geometry and RPM metadata to seed spectral priors; large operating-point excursions or configuration changes may require re-calibration. Our experiments focus on rotating machinery with vibration sensing and do not yet cover other asset classes or heterogeneous sensing modalities. Future work will aim to: (i) develop self-calibrating priors via online identification and RPM compensation so that spectral bands track operating conditions automatically; (ii) extend cross-

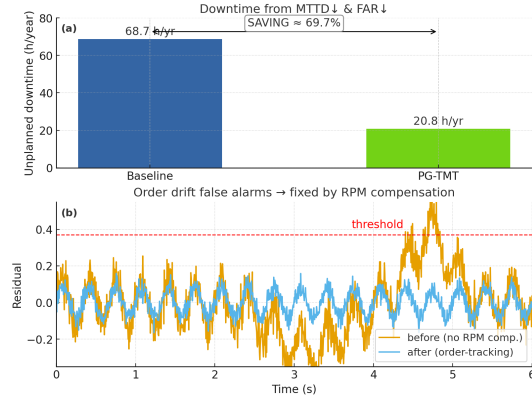


Fig. 9. Pilot benefit: downtime reduction due to earlier detection (lower MTTD at matched intensity) and fewer nuisance alarms via RPM-aware compensation.

TABLE IV
ACCURACY UNDER ADDITIVE NOISE: PR-AUC AND ROC-AUC
(MEAN \pm 95% CI) OVER LEAKAGE-FREE STREAMING RUNS.

Dataset	SNR (dB)	PR-AUC	ROC-AUC	#Runs
CWRU	clean	0.964 \pm 0.007	0.992 \pm 0.003	5
	20	0.958 \pm 0.010	0.989 \pm 0.004	5
	15	0.947 \pm 0.012	0.985 \pm 0.005	5
	10	0.931 \pm 0.016	0.980 \pm 0.006	5
	5	0.905 \pm 0.020	0.970 \pm 0.009	5
	0	0.862 \pm 0.028	0.946 \pm 0.012	5
Paderborn (PU)	clean	0.952 \pm 0.008	0.986 \pm 0.004	5
	20	0.945 \pm 0.010	0.984 \pm 0.004	5
	15	0.936 \pm 0.012	0.980 \pm 0.005	5
	10	0.918 \pm 0.016	0.973 \pm 0.007	5
	5	0.889 \pm 0.021	0.962 \pm 0.010	5
	0	0.838 \pm 0.030	0.935 \pm 0.014	5
XJTU-SY	clean	0.946 \pm 0.009	0.984 \pm 0.004	5
	20	0.939 \pm 0.011	0.981 \pm 0.005	5
	15	0.927 \pm 0.013	0.977 \pm 0.006	5
	10	0.909 \pm 0.017	0.970 \pm 0.008	5
	5	0.876 \pm 0.022	0.959 \pm 0.011	5
	0	0.821 \pm 0.031	0.928 \pm 0.015	5

points are matched by EVT thresholds with hysteresis; SNR sweeps hold thresholds fixed at a high-SNR reference.

TABLE V
EARLY DETECTION AND ROBUSTNESS UNDER ADDITIVE NOISE:
MEAN \pm 95% CI OF MTTD AND FAR (EPISODES/HOUR).

Dataset	SNR (dB)	MTTD (s)	FAR (events/hour)	Refractory	ΔT_{merge} (s)
CWRU	clean	27.8 \pm 3.5	0.18 \pm 0.05	2.0	
	20	29.4 \pm 3.8	0.20 \pm 0.05	2.0	
	15	31.7 \pm 4.2	0.24 \pm 0.06	2.0	
	10	35.9 \pm 4.8	0.31 \pm 0.07	2.0	
	5	41.2 \pm 5.6	0.44 \pm 0.10	2.0	
	0	49.6 \pm 6.8	0.63 \pm 0.12	2.0	
Paderborn (PU)	clean	30.6 \pm 3.7	0.22 \pm 0.06	2.0	
	20	32.1 \pm 4.0	0.25 \pm 0.06	2.0	
	15	34.8 \pm 4.4	0.29 \pm 0.07	2.0	
	10	39.7 \pm 5.1	0.38 \pm 0.09	2.0	
	5	46.5 \pm 6.1	0.52 \pm 0.12	2.0	
	0	56.2 \pm 7.5	0.71 \pm 0.13	2.0	
XJTU-SY	clean	33.4 \pm 3.9	0.24 \pm 0.06	2.0	
	20	35.2 \pm 4.2	0.27 \pm 0.06	2.0	
	15	38.1 \pm 4.6	0.32 \pm 0.07	2.0	
	10	43.6 \pm 5.4	0.42 \pm 0.10	2.0	
	5	51.4 \pm 6.6	0.58 \pm 0.12	2.0	
	0	61.3 \pm 8.2	0.78 \pm 0.15	2.0	

is computed under the streaming protocol with right-censoring of missed events. FAR counts unique alarm episodes per hour after hysteresis and refractory merging with $\Delta T_{\text{merge}} = 2.0$ s; the same refractory window is used for all methods.

domain/sensor adaptation to heterogeneous rigs and multi-asset fleets with stronger cross-asset generalization; (iii) incorporate uncertainty quantification for EVT and score calibration to better support risk-aware maintenance decisions under covariate shift; and (iv) further integrate the backbone-agnostic reliability layer with ONNX/TensorRT pipelines and fleet-level KPIs, so that life-cycle benefits can be assessed and audited at scale. We hope that releasing code, manifests, and deployment artifacts will facilitate reuse of this early-warning framework in broader PHM and industrial reliability studies.

REFERENCES

- [1] Y. Lei, N. Li, L. Guo, T. Yan, and J. Lin, "Machinery health condition monitoring and fault diagnosis using deep learning techniques: A review," *Mech. Syst. Signal Process.*, vols. 76–77, pp. 231–265, 2016, DOI: [10.1016/j.ymssp.2016.02.016](https://doi.org/10.1016/j.ymssp.2016.02.016).
- [2] Z. Zhu, Y. Chen, F. Zhou, X. He, and Y. Liu, "A review of the application of deep learning in intelligent fault diagnosis for rotating machinery," *Measurement*, vol. 210, 112353, 2023, DOI: [10.1016/j.measurement.2022.112353](https://doi.org/10.1016/j.measurement.2022.112353).
- [3] O. Das, S. N. Omkar, and S. Dey, "Machine learning for fault analysis in rotating machinery: A review," *Sci. Rep.*, vol. 13, 10223, 2023, DOI: [10.1038/s41598-023-37159-0](https://doi.org/10.1038/s41598-023-37159-0).
- [4] J. Antoni, "The spectral kurtosis: A useful tool for characterising non-stationary signals," *Mech. Syst. Signal Process.*, vol. 20, no. 2, pp. 282–307, 2006, DOI: [10.1016/j.ymssp.2005.02.001](https://doi.org/10.1016/j.ymssp.2005.02.001).
- [5] J. Antoni, "Cyclostationarity by examples," *Mech. Syst. Signal Process.*, vol. 21, no. 2, pp. 597–630, 2007, DOI: [10.1016/j.ymssp.2006.03.006](https://doi.org/10.1016/j.ymssp.2006.03.006).
- [6] R. B. Randall and J. Antoni, "Rolling element bearing diagnostics—A tutorial," *Mech. Syst. Signal Process.*, vol. 25, no. 2, pp. 485–520, 2011, DOI: [10.1016/j.ymssp.2010.07.017](https://doi.org/10.1016/j.ymssp.2010.07.017).
- [7] P. D. McFadden and J. D. Smith, "Model for the vibration produced by a single point defect in a rolling element bearing," *J. Sound Vib.*, vol. 96, no. 1, pp. 69–82, 1984, DOI: [10.1016/0022-460X\(84\)90595-9](https://doi.org/10.1016/0022-460X(84)90595-9).
- [8] A. Gu and T. Dao, "Mamba: Linear-time sequence modeling with selective state spaces," *arXiv preprint arXiv:2312.00752*, 2023, DOI: [10.48550/arXiv.2312.00752](https://doi.org/10.48550/arXiv.2312.00752).
- [9] A. Gu, K. Goel, and C. Ré, "Efficiently modeling long sequences with structured state spaces," *arXiv preprint arXiv:2111.00396*, 2022, DOI: [10.48550/arXiv.2111.00396](https://doi.org/10.48550/arXiv.2111.00396).
- [10] J. T. H. Smith, A. J. Warrington, and S. W. Linderman, "Simplified state space layers for sequence modeling (S5)," *arXiv preprint arXiv:2208.04933*, 2022, DOI: [10.48550/arXiv.2208.04933](https://doi.org/10.48550/arXiv.2208.04933).
- [11] A. Vaswani, N. Shazeer, et al., "Attention is all you need," in *Proc. NeurIPS*, 2017, pp. 5998–6008, DOI: [10.48550/arXiv.1706.03762](https://doi.org/10.48550/arXiv.1706.03762).
- [12] A. Dosovitskiy, et al., "An image is worth 16 \times 16 words: Transformers for image recognition at scale," in *Proc. ICLR*, 2021, DOI: [10.48550/arXiv.2010.11929](https://doi.org/10.48550/arXiv.2010.11929).
- [13] G. E. Karniadakis, I. G. Kevrekidis, L. Lu, P. Perdikaris, S. Wang, and L. Yang, "Physics-informed machine learning," *Nature Rev. Phys.*, vol. 3, no. 6, pp. 422–440, Jun. 2021, DOI: [10.1038/s42254-021-00314-5](https://doi.org/10.1038/s42254-021-00314-5).
- [14] M. Raissi, P. Perdikaris, and G. E. Karniadakis, "Physics-informed neural networks: A deep learning framework for solving forward and inverse problems involving nonlinear PDEs," *J. Comput. Phys.*, vol. 378, pp. 686–707, 2019, DOI: [10.1016/j.jcp.2018.10.045](https://doi.org/10.1016/j.jcp.2018.10.045).
- [15] S. L. Brunton, J. L. Proctor, and J. N. Kutz, "Discovering governing equations from data by sparse identification of nonlinear dynamical systems," *Proc. Natl. Acad. Sci. USA*, vol. 113, no. 15, pp. 3932–3937, 2016, DOI: [10.1073/pnas.1517384113](https://doi.org/10.1073/pnas.1517384113).
- [16] A. Siffrer, P.-A. Fouque, A. Termier, and C. Largouët, "Anomaly detection in streams with extreme value theory," in *Proc. KDD*, 2017, pp. 1067–1075, DOI: [10.1145/3097983.3098144](https://doi.org/10.1145/3097983.3098144).
- [17] E. Vignotto and S. Engelke, "Extreme value theory for anomaly detection: The GPD classifier," *Stat. Comput.*, vol. 30, pp. 185–205, 2020, DOI: [10.1007/s11222-020-09938-7](https://doi.org/10.1007/s11222-020-09938-7).
- [18] T. Saito and M. Rehmsmeier, "The precision–recall plot is more informative than the ROC plot when evaluating binary classifiers on imbalanced datasets," *PLoS ONE*, vol. 10, no. 3, e0118432, 2015, DOI: [10.1371/journal.pone.0118432](https://doi.org/10.1371/journal.pone.0118432).
- [19] A. Lavin and S. Ahmad, "Evaluating real-time anomaly detection algorithms—The Numenta anomaly benchmark," in *Proc. IEEE ICMLA*, 2015, pp. 38–44, DOI: [10.1109/ICMLA.2015.141](https://doi.org/10.1109/ICMLA.2015.141).

[20] H. Xu, Y. Wang, Z. Jiang, *et al.*, “Anomaly Transformer: Time series anomaly detection with association discrepancy,” in *Proc. ICLR*, 2022, DOI: 10.48550/arXiv.2110.02642.

[21] NVIDIA, *TensorRT Developer Guide*, 2022. [Online]. Available: <https://docs.nvidia.com/deeplearning/tensorrt/archives/tensorrt-843/pdf/TensorRT-Developer-Guide.pdf> (accessed Oct. 25, 2025).

[22] J. Hendriks, V. Knaepen, K. Janssens, and W. Desmet, “Towards better benchmarking using the CWRU bearing dataset,” *Mech. Syst. Signal Process.*, vol. 162, 108033, 2022, DOI: 10.1016/j.ymssp.2021.108033.

[23] W. A. Smith and R. B. Randall, “Rolling element bearing diagnostics using the Case Western Reserve University data: A benchmark study,” *Mech. Syst. Signal Process.*, vols. 64–65, pp. 100–131, 2015, DOI: 10.1016/j.ymssp.2015.04.021.

[24] C. Lessmeier, J. K. Kimotho, D. Zimmer, and W. Sextro, “Condition monitoring of bearing damage in electromechanical drive systems by using the Paderborn University dataset,” in *Proc. PHM Society Eur. Conf. (PHME)*, 2016. [Online]. Available: <https://mb.uni-paderborn.de/kat/forschung/datensets-bilder>

[25] Y. Lei, T. Han, B. Wang, N. Li, T. Yan, and J. Yang, “XJTU-SY rolling element bearing accelerated life test datasets: A tutorial,” *J. Mech. Eng.*, vol. 55, no. 16, pp. 1–6, 2019, DOI: 10.3901/JME.2019.16.001.

[26] S. J. Pan and Q. Yang, “A survey on transfer learning,” *IEEE Trans. Knowl. Data Eng.*, vol. 22, no. 10, pp. 1345–1359, Oct. 2010, DOI: 10.1109/TKDE.2009.191.

[27] Y. Ganin, E. Ustinova, *et al.*, “Domain-adversarial training of neural networks,” *J. Mach. Learn. Res.*, vol. 17, no. 59, pp. 1–35, 2016. [Online]. Available: <https://jmlr.org/papers/v17/15-239.html>

[28] E. Tzeng, J. Hoffman, K. Saenko, and T. Darrell, “Adversarial discriminative domain adaptation,” in *Proc. CVPR*, 2017, pp. 7167–7176, DOI: 10.1109/CVPR.2017.634.

[29] W. Lin and G. Michailidis, “Deep learning-based approaches for state-space models: A selective review,” *arXiv preprint arXiv:2412.11211*, 2024, DOI: 10.48550/arXiv.2412.11211.

[30] Y. Su, Y. Zhao, C. N. C. Leung, M. Pei, and D. Miao, “Robust anomaly detection for multivariate time series through stochastic recurrent neural network,” in *Proc. KDD*, 2019, pp. 2828–2837, DOI: 10.1145/3292500.3330672.

[31] Q. Yao, Z. Wang, F. Gao, and X. Li, “A bearing fault diagnosis method based on envelope order tracking and spectral kurtosis,” *IEEE Trans. Instrum. Meas.*, vol. 68, no. 11, pp. 4310–4320, Nov. 2019, DOI: 10.1109/TIM.2019.2898821.

[32] Y. Cheng, H. Zhang, and J. Qin, “Wasserstein distance-based deep adversarial transfer learning for intelligent fault diagnosis,” *IEEE Trans. Ind. Inf.*, vol. 15, no. 9, pp. 5099–5110, Sep. 2019, DOI: 10.1109/TII.2019.2909875.

[33] S. Shao, S. McAleer, R. Yan, and P. Baldi, “Highly accurate machine fault diagnosis using deep transfer learning,” *IEEE Trans. Ind. Inf.*, vol. 15, no. 4, pp. 2446–2455, Apr. 2019, DOI: 10.1109/TII.2018.2877209.

[34] H. Zhong, Z. Yang, R. Wang, and X. Li, “Bearing fault diagnosis using transfer learning and self-attention,” *Neurocomputing*, vol. 487, pp. 315–327, 2022, DOI: 10.1016/j.neucom.2021.12.059.

[35] Y. Xiao, H. Shao, J. Wang, S. Yan, and B. Liu, “Bayesian variational Transformer: A generalizable model for rotating machinery fault diagnosis,” *Mech. Syst. Signal Process.*, vol. 205, 110696, 2024, DOI: 10.1016/j.ymssp.2023.110696.

[36] E. L. Kaplan and P. Meier, “Nonparametric Estimation from Incomplete Observations,” *J. Am. Stat. Assoc.*, vol. 53, no. 282, pp. 457–481, 1958, DOI: 10.1080/01621459.1958.10501452.

[37] D. R. Cox, “Regression models and life-tables,” *J. R. Stat. Soc. Ser. B*, vol. 34, no. 2, pp. 187–220, 1972.

[38] Y. Benjamini and Y. Hochberg, “Controlling the false discovery rate: A practical and powerful approach to multiple testing,” *J. R. Stat. Soc. Ser. B*, vol. 57, no. 1, pp. 289–300, 1995, DOI: 10.1111/j.2517-6161.1995.tb02031.x.

[39] E. R. DeLong, D. M. DeLong, and D. L. Clarke-Pearson, “Comparing the areas under two or more correlated ROC curves: A nonparametric approach,” *Biometrics*, vol. 44, no. 3, pp. 837–845, 1988, DOI: 10.2307/2531595.

[40] C. Guo, G. Pleiss, Y. Sun, and K. Q. Weinberger, “On calibration of modern neural networks,” in *Proc. ICML*, 2017, pp. 1321–1330.

[41] A. N. Angelopoulos and S. Bates, “A gentle introduction to conformal prediction and distribution-free uncertainty quantification,” *arXiv preprint arXiv:2107.07511*, 2023.

[42] X.-S. Si, W. Wang, C.-H. Hu, and D.-H. Zhou, “Remaining useful life estimation—A review on the statistical data-driven approaches,” *Eur. J. Oper. Res.*, vol. 213, no. 1, pp. 1–14, 2011, DOI: 10.1016/j.ejor.2010.11.018.

[43] X.-S. Si, W. Wang, C.-H. Hu, D.-H. Zhou, and M. G. Pecht, “Remaining useful life estimation based on a nonlinear diffusion degradation process,” *IEEE Trans. Reliab.*, vol. 61, no. 1, pp. 50–67, 2012, DOI: 10.1109/TR.2011.2182221.

[44] Z.-S. Ye, Y. Wang, K.-L. Tsui, and M. Pecht, “Degradation data analysis using Wiener processes with measurement errors,” *IEEE Trans. Reliab.*, vol. 62, no. 4, pp. 772–780, 2013.

[45] K. Feldman, D. Jazouli, and P. Sandborn, “A methodology for determining the return on investment associated with PHM,” *IEEE Trans. Reliab.*, vol. 58, no. 2, pp. 305–316, 2009, DOI: 10.1109/TR.2009.2020133.

[46] M. Compare, L. Bellani, and E. Zio, “Availability model of a PHM-equipped component,” *IEEE Trans. Reliab.*, vol. 66, no. 2, pp. 487–501, 2017, DOI: 10.1109/TR.2017.2669400.

[47] J. Gama, I. Žliobaité, A. Bifet, M. Pechenizkiy, and A. Bouchachia, “A survey on concept drift adaptation,” *ACM Comput. Surv.*, vol. 46, no. 4, 2014, DOI: 10.1145/2523813.

[48] Z. Zhang, N. Chen, and Z.-S. Ye, “Degradation data analysis and remaining useful life estimation: A review on Wiener-process-based methods,” *Eur. J. Oper. Res.*, vol. 271, no. 3, pp. 775–796, 2018, DOI: 10.1016/j.ejor.2018.03.030.

[49] D. Wang, C. Miao, X. Ma, K. L. Tsui, and M. Pecht, “Online anomaly detection for hard disk drives based on Mahalanobis distance,” *IEEE Trans. Reliab.*, vol. 62, no. 1, pp. 136–145, 2013, DOI: 10.1109/TR.2013.2241204.

[50] B. Sun, S. Zeng, R. Kang, and M. G. Pecht, “Benefits and challenges of system prognostics,” *IEEE Trans. Reliab.*, vol. 61, no. 2, pp. 323–335, 2012, DOI: 10.1109/TR.2012.2194173.

Changyu Li is a research intern with the IoT and Smart Sensing Lab at Great Bay University (supervised by Prof. Fei Luo). His interests include embodied AI, mechanical engineering, industrial condition monitoring, and AI for Science. He works on efficient hybrid state-space/Transformer models for early fault detection and edge deployment.



Dingcheng Huang is a Ph.D. candidate in Mechanical Engineering at the Massachusetts Institute of Technology (MIT). He received the S.M. degree in Mechanical Engineering from MIT in 2025 and the B.S. degree in Mechanical Engineering from Northwestern University in 2023. His research interests include human-robot collaboration, intelligent autonomous systems, real-time perception, dynamic motion planning, and multi-objective optimization.



Kexuan Yao is a doctoral candidate at the Institute of Aircraft Propulsion Technology, School of Aerospace Engineering, Zhejiang University. He received the B.S. degree in Mechanics and Aerospace Engineering from Southern University of Science and Technology (SUSTech) in 2022 and the M.S. degree from Moscow Aviation Institute (MAI) in 2024. His research focuses on new-energy low-altitude aircraft, including system design, parametric modeling, and integrated performance optimization.





Xiaoya Ni is a Master's student at the National University of Singapore (NUS). She received the B.Eng. degree from the School of Mechanical and Electrical Engineering, Soochow University. Her interests include mechatronics and robotics, with emphasis on perception-control integration for intelligent machines.



Lijuan Shen is a Senior Lecturer in Data Science at the School of Science and Technology, James Cook University (Singapore Campus). Her research bridges data science and systems resilience, focusing on data-driven approaches to assess and enhance the resilience of complex infrastructure systems. She has published over 40 papers in journals including *IEEE Transactions on Reliability*, *IIE Transactions*, *Journal of Quality Technology*, *Reliability Engineering & System Safety*, and *International Journal of Production Economics*. She received an NRF (Singapore) grant in 2021 and has served as Guest Editor for *Quality and Reliability Engineering International*.



Fei Luo is an Assistant Professor of Computer Science at Great Bay University, Dongguan, China (e-mail: luofei@gbu.edu.cn). His research focuses on human activity recognition, wireless sensing, edge intelligence, and multimodal fusion. He has published 14 papers (11 as first/corresponding author), holds 1 invention patent, and leads a National Natural Science Foundation of China Young Scientist project.

He received the B.Sc. degree in Geographic Information Systems from Jiangxi University of Science and Technology in 2012, the M.Sc. degree in Surveying and Mapping from Wuhan University in 2016, and the Ph.D. degree in Electronic Engineering from Queen Mary University of London in 2020. He has served as a GIS developer at the Chinese Academy of Surveying and Mapping, a Postdoctoral Researcher at Shenzhen University, and a Chief Engineer at Honor Device Co., Ltd., Shenzhen. He is a visiting scholar at the Hong Kong University of Science and Technology (Guangzhou) and has reviewed for *IEEE TMC*, *IEEE IoTJ*, *IEEE TNNLS*, and *IEEE Sensors*. He was twice a student ambassador for the IET Faraday Challenge Day.